Available online at www.sciencedirect.com

SciVerse ScienceDirect

Energy Procedia 00 (2016) 000–000

Energy Procedia

www.elsevier.com/locate/procedia

13th Deep Sea Offshore Wind R&D Conference, EERA DeepWind'2016, 20-22 January 2016, Trondheim, Norway

Wind coherence measurement by a single pulsed Doppler wind lidar

Etienne Cheynet[a,*], Jasna Bogunović Jakobsen[a], Benny Svardal[b], Joachim Reuder[c], Valerie Kumer[c]

[a] *Department of Mechanical and Structural Engineering and Materials Science, University of Stavanger, N-4036 Stavanger, Norway*
[b] *Christian Michelsen Research AS, Fantoftveien 38, Bergen, Norway*
[c] *Geophysical Institute, University of Bergen, Allegaten 70, N-5007 Bergen, Norway*

Abstract

A single pulsed Doppler wind lidar, deployed at the FINO1 platform in the North Sea, has been used to monitor the lateral and vertical coherence of the along-wind component. To maximize the sampling frequency of the monitoring system, a particular configuration based on small sweeping angles around the mean wind direction is used. The set-up provides wind velocity measurement with an increasing cross-flow separation with increasing distances from the lidar. We present hereby preliminary results from the analysis of the Plan Position Indicator scans carried out with a sampling frequency of 0.13 Hz, and the Range Height Indicator scans sampled at 0.19 Hz. The mean velocity and the turbulence intensity indicated a sufficiently uniform flow, which was verified by the calculation of the along and crosswind turbulence length scales. The lateral and vertical coherence was estimated based on multiple 10-minutes samples, for a mean wind velocity ranging from 10 to 14 m s^{-1}. For the conditions examined, the measured coherence showed a good agreement with the IEC model for low and medium cross-flow separations, and a fairly good agreement with the Frøya model for large separations.

Peer-review under responsibility of SINTEF Energi AS.

Keywords:
Pulsed wind lidar, FINO1, Offshore wind, Coherence, Wind turbulence, Wind load, Wind turbine

1. Introduction

The co-coherence is used to quantify the in-phase correlation of the wind velocity fluctuations and is therefore a governing parameter to estimate wind loads on structures. A more accurate description of the lateral and vertical co-coherence for the along-wind component may become necessary for offshore wind turbines considering the increasing diameters of blades. Unfortunately, full scale measurements of the co-coherence remains sparse in the literature. The lateral co-coherence has been traditionally measured for applications on long-span bridges [1–3], while vertical coherence has been mainly studied on flat terrain for towers, high-rise buildings and chimneys [4,5]. To study dynamic wind loads on wind turbines, both the lateral and the vertical coherence is required. To the authors knowledge, only

* Corresponding author. Tel.: +4793824306.
E-mail address: etienne.cheynet@uis.no

Peer-review under responsibility of SINTEF Energi AS.

in [6,7] both lateral and vertical coherence in conditions representative for offshore areas have been addressed. The limited lateral separations accessible by mast measurements may be overcome by the use of Doppler wind lidars, but their applications for coherence measurement remains unexplored so far. A system of multiple-wind lidars is desirable to study wind coherence, by allowing the use of a higher sampling frequency than with a single lidar and the retrieval of the different wind components [8–11].

However, if only a single wind lidar is available, measuring the wind coherence becomes more challenging and only the along-beam coherence has been studied so far [12,13]. We present hereby a novel measurement set-up based on a single scanning pulsed Doppler wind lidar to measure lateral and vertical wind coherence of the along-wind component. A WindCube 100S, deployed at an altitude of 25 m at the FINO1 platform in the North Sea, was used during one week in December 2015 for this purpose. Application of wind lidar technology to monitor the wind field near FINO1 is not new, as highlighted by e.g. [14–17]. However, this is the first time that such configuration provides both a temporal and spatial resolution high enough to explore the single and two-point statistics of the along-wind turbulence, for cross-flow separations that cannot be covered by the traditional wind masts.

The main goal of the present study is to assess the potential of a single Doppler wind lidar to measure wind coherence. In the following, the configurations and working assumptions are discussed first. Some preliminary results are then given, demonstrating the proof of concept. Finally, the root-coherence of the along-wind component is compared to semi-empirical models from the literature for different vertical and lateral separations.

2. Monitoring system and methods

2.1. Measurement site and instrumentation

Doppler wind lidars are remote sensing devices used for wind velocity measurement using Doppler frequency shift of light backscattered from aerosols. In the present study, a WindCube 100S from Leosphere is used. The instrument is a pulsed Doppler wind lidar with a rotating head enabling hemispherical scans. The word "scan" refers here to the sweeping process carried out continuously during 10-minutes by the lidar to record time series of the wind velocity. The WindCube 100S has been previously used as wind profiler [18], to study wind turbulence in complex terrain [11], or to monitor the wake of onshore wind turbines [19]. Two scanning patterns are hereby used: the Plan Position Indicator (PPI) and the Range Height Indicator (RHI) as highlighted by the schematic view in Fig. 1 where z is the vertical axis, x is the horizontal axis parallel to the wind direction, ϕ is the azimuth angle, α is the elevation angle, and r is the radial distance from the lidar. In Fig. 1, $\overrightarrow{t}$ is the unit vector tangent to the curve defined by the motion of the scanning head, and $\overrightarrow{n}$ is the unit vector normal to $\overrightarrow{t}$ and oriented towards the centre of the arc. The PPI scan is carried out for a fixed elevation, and multiple azimuth angles. The RHI scan is run for a single azimuth, and multiple elevation angles. If both the azimuth and the elevation angles are fixed, the lidar operates in Line Of Sight (LOS) mode. The azimuth angle is defined as the angle between the projection of the beam onto the horizontal plane and the North, whereas the elevation angle is defined as the angle between the beam and its projection onto the horizontal plane. The yaw angle β is defined as the angle between the wind direction and the azimuth angle, and consequently, a zero yaw angle indicates that the beam is aligned with the wind direction whereas a yaw angle of 90° indicates that the beam is perpendicular to the wind direction. The yaw angle β can be divided into two contributions: a yaw angle β_a introduced by an initial misalignment between the lidar beam and the wind direction, and a yaw angle β_s due to the sweeping of the beam around the mean wind direction during the PPI scan:

$$\beta = \beta_a + \beta_s \tag{1}$$

The research platform FINO1 is located to the north of Borkum (Germany) in the North Sea. As a part of the OBLEX-F1 campaign, a WindCube 100S was installed on the South-West part of the FINO1 platform in May 2015. In December 2015, exploratory tests were dedicated to coherence measurement by using PPI and RHI scans with configurations summarized in Table 1. The mean wind velocity and direction recorded by anemometers located at 33, 40, 50, 60, 70, 80 and 90 m above the sea and installed on a wind mast at the FINO1 platform are used as reference data. During the week studied, the Lidar was manually oriented to scan in PPI mode over a small sector centred on an azimuth of 211°, which was equal to the main wind direction according to the reference anemometers. For the RHI

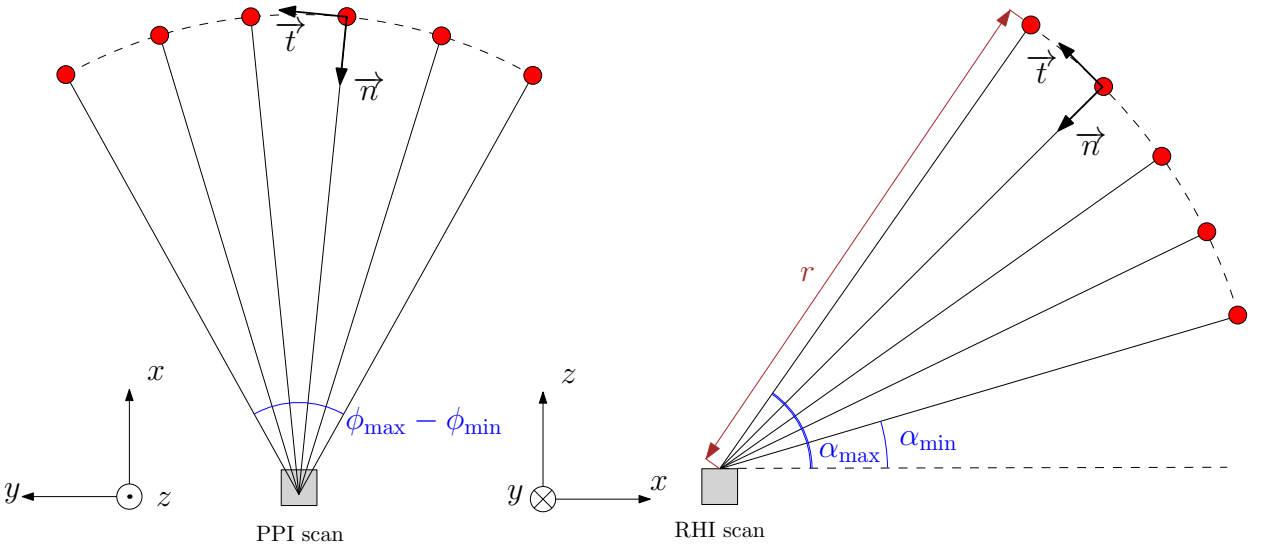

Fig. 1. Schematic of the PPI scan (left) and of the RHI scan (right), with magnified angle to improve the clarity.

Table 1. Parameters used for each scanning scenario.

Parameters	PPI	RHI
Azimuth (°)	208 to 214	211
Elevation (°)	0	0 to 4
Sampling frequency (Hz)	0.13	0.19
Scan speed (° s^{-1})	0.6	0.8
Accumulation time (s)	0.5	0.5
Total duration (s)	585	585
Effective distance (m)	50 to 1500	50 to 1500
Gate range (m)	25	25
Carrier to Noise Ratio threshold (dB)	-23	-23

scan, the azimuth was also fixed to 211°. If the wind direction is equal to 211°, the lidar may record the far-wake of at least one wind turbine, located around 30 rotor diameters from FINO1 (Fig. 2). According to Højstrup [7], consequences on coherence measurement should however be limited.

Because the lidar records the radial wind velocity component in a plane, a "grid" can be defined for each PPI and RHI scan, where each node of the grid is defined by a unique triple $\{\phi, \alpha, r\}$. Time series of the radial wind velocity are studied here in 354 nodes for the PPI scan and in 472 nodes for the RHI scan. The sampling is equally spaced in time at the centre of the scanned area, but alternates between a short and a long sampling interval towards the edges. A re-sampling of the time series is therefore necessary for a more efficient handling of the wind data.

2.2. *Working assumptions*

Following Teunissen [20], the along-wind component U is assumed to be entirely described by a mean part, $\overline{U}$, and a fluctuating part with zero mean, u. A similar definition is done for the radial wind velocity component V_r:

$$\begin{aligned} U &= \overline{U} + u \\ V_r &= \overline{V}_r + v_r \end{aligned} \tag{2}$$

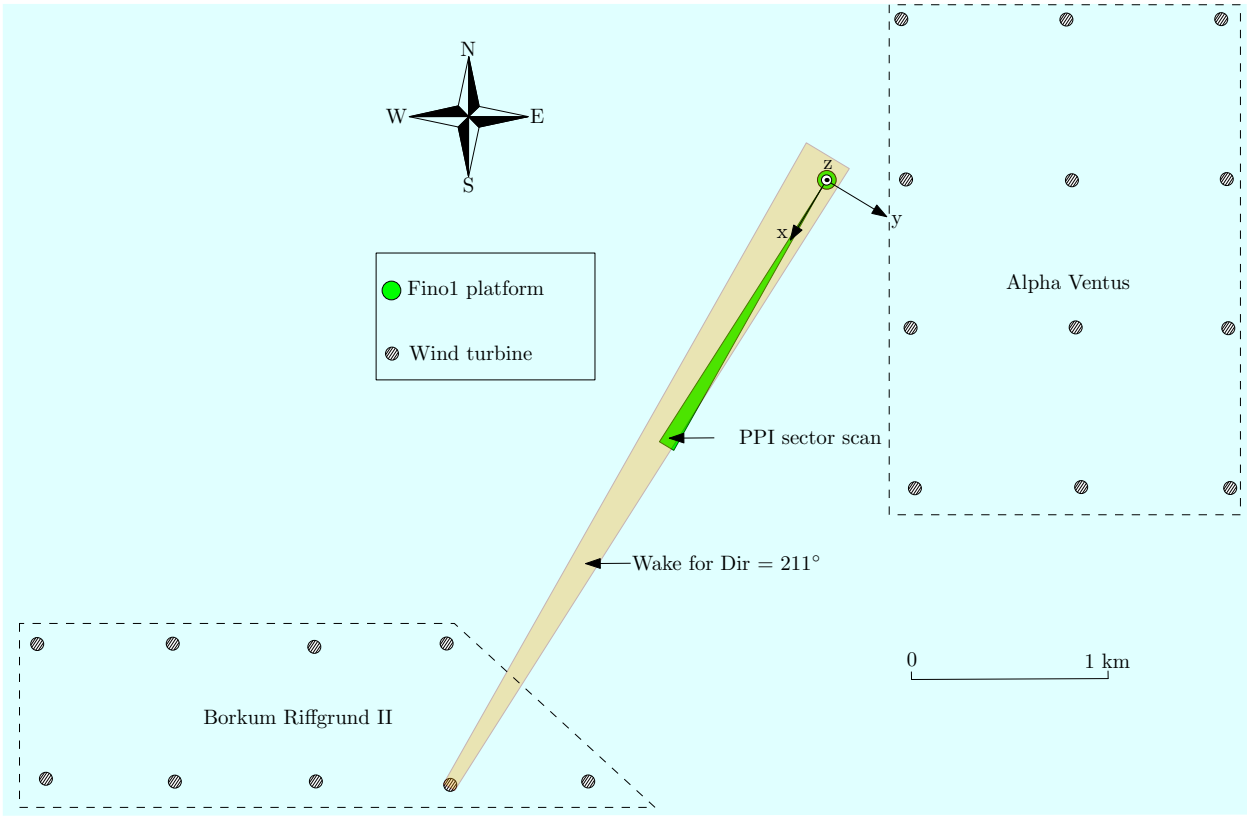

Fig. 2. Schematic of the position of the FINO1 platform and the position of the wind turbines relative to the scanning wind lidar.

In this subsection, the yaw angle β_a is assumed to be equal to zero, and Eq. 1 becomes $\beta = \beta_s$. In other words, non-zero yaw angles β are only due to the periodic sweeping of the beam during the PPI scan. For small yaw, small elevations angles and the large scanning distances, a line segment can approximate the arc created by the scanning beam. If the scanned area is "centred" around the mean wind direction, the tangential direction $\overrightarrow{t}$ is assumed to be parallel to the cross-flow direction, and the vector $\overrightarrow{n}$ is parallel to the wind direction (Fig. 1). The scanning beams are therefore almost parallel, and the radial wind velocity component can be assumed equal to the along-wind component. The relative error due to this assumption is estimated for the first two statistical moments of the radial wind component. To assess this error, the relation between the standard deviation of the along-wind, across-wind and vertical wind components denoted σ_u, σ_v and σ_w respectively, is approximated following Holmes [21] by:

$$\begin{aligned} \sigma_v &= 0.9 \cdot \sigma_u \\ \sigma_w &= 0.6 \cdot \sigma_u \end{aligned} \tag{3}$$

For the RHI scan, the relation between V_r and U is given by:

$$V_r = U\cos(\alpha) + W\sin(\alpha) \tag{4}$$

The relative error ϵ due to the assumption $\overline{V}_r \simeq \overline{U}$ is therefore:

$$\epsilon = \frac{1}{\cos(\alpha)} - 1 \tag{5}$$

and for $\sigma_{v_r} \simeq \sigma_u$:

$$\epsilon = \frac{1}{\cos(\alpha) + 0.6\sin(\alpha)} - 1 \tag{6}$$

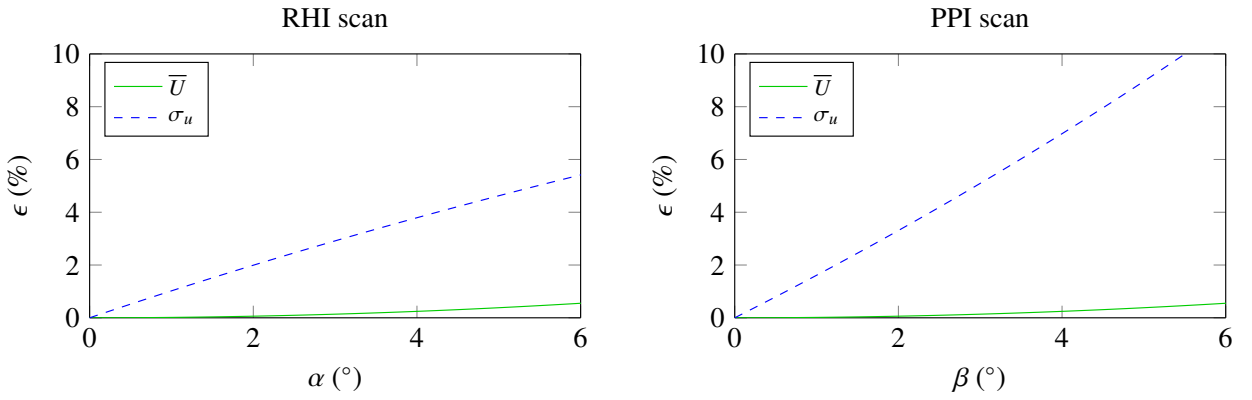

Fig. 3. Relative error ϵ expressed as a function of the elevation angle α (left) and the yaw angle β (right), displayed for the first two statistical moments of the along-wind component.

For the PPI scan, the relation between V_r and U is obtained using:

$$V_r = U\cos(\beta) - V\sin(\beta) \tag{7}$$

The error induced by $\overline{V}_r \simeq \overline{U}$ for the PPI scan is :

$$\epsilon = \frac{1}{\cos(\beta)} - 1 \tag{8}$$

and for $\sigma_{v_r} \simeq \sigma_u$:

$$\epsilon = \frac{1}{\cos(\beta) - 0.9\sin(\beta)} - 1 \tag{9}$$

For elevation and yaw angles up to 6°, the relative error remains lower than 1 % for the mean wind velocity. However, it is higher for the standard deviation (Fig. 3). For the PPI scan, the error for σ_u stays below 10 % if the yaw angle is lower than 5.5°. For the RHI scan, if a maximum elevation angle of 4° is used, V_r can be assumed to be equal to U, provided that the lidar beam is aligned with the wind direction. Similarly for the PPI scan, if the scanned area is "centred" around the mean wind direction, then a yaw angle of 3° is small enough to consider that $V_r \simeq U$. The larger error for the PPI scan is mainly due to the larger multiplying factor in Eq. 3 between σ_u and σ_v than between σ_u and σ_w.

2.3. Turbulence length scales

The streamwise turbulence length scale for the along-wind component is denoted L_u^x, and is calculated from the integral time scale [22], by assuming that Taylor's hypothesis of frozen turbulence can be applied. Following the method proposed by [23], L_u^x is estimated by integrating the single-sided auto-covariance function of the fluctuating wind velocity R_u up to the first zero crossing:

$$L_u^x = \overline{U} \cdot \int_{t=0}^{t(R_u(t)=0)} R_u(t)\,\mathrm{d}t \tag{10}$$

In the present study, L_u^x is used as an indicator of the wind field homogeneity. It is therefore calculated for each volume scanned during the PPI and RHI scan. If large fluctuations of L_u^x are recorded, it may indicate a non-stationary flow, a non-uniform wind field or an unusually low Carrier to Noise Ratio (CNR). The CNR is here defined as the signal to noise ratio (SNR) on the carrier frequency. In the present study, a threshold value of -23 dB is used, as advised by [18,24], leading to good quality data up to at least 1.5 km far from the lidar.

For a given radial distance r, the turbulence length scale of the u-component for separations in the y-direction is denoted L_u^y and is calculated using the PPI scanning mode. Similarly, L_u^z is calculated in the z-direction based on the RHI scanning mode. These length scales are estimated by computing the auto-covariance function R_{uu} of the along-wind component for cross-flow separations, which is then integrated following:

$$L_u^s = \int_0^{+\infty} R_{uu}(s)\,\mathrm{d}s \tag{11}$$

where $s = \{y, z\}$. As L_u^y and L_u^z are calculated for multiple positions along the beam, they can be used to quantify the evolution of the coherence for lateral and vertical separation with increasing radial distance r from the lidar.

2.4. Spectral coherence

Following the notations of Davenport [25], the normalized cross-spectral density of the wind fluctuations simultaneously measured at two positions s_p and s_q is denoted $\boldsymbol{R}_{pq}$ and is defined as:

$$\boldsymbol{R}_{pq}(f) = \frac{\left|\mathbf{S}_{pq}(f)\right|}{\sqrt{\mathbf{S}_{pp}(f)\cdot\mathbf{S}_{qq}(f)}} = \sqrt{\mathbf{Co}_{pq}^2(f) + \mathbf{Qu}_{pq}^2(f)} \tag{12}$$

in which $\mathbf{S}_{pq}$ is the cross-spectral density of wind velocity fluctuations between positions s_p and s_q, and $\mathbf{S}_{pp}$ and $\mathbf{S}_{qq}$ are the auto-spectral densities at positions s_p and s_q respectively. $\mathbf{Co}_{pq}$ and $\mathbf{Qu}_{pq}$ are the co-coherence and quad-coherence of the velocity fluctuations respectively, defined for a given frequency f, and a spatial separation $d = \left|s_p - s_q\right|$. In the present study, the co-coherence is approximated by the root-coherence, which is utilized when estimating wind loads on wind turbines, and frequently for other structures [26]. In the following, the root-coherence function for the along-wind component is denoted by γ_u.

The coherence is calculated by using Welch's overlapped segment averaging estimator [27]. Records of 10 minutes divided into blocks of 150 second are used with 50% overlapping as suggested by [5,28]. This aims to reduce the measurement noise and the bias of the coherence estimate. The lowest recorded frequency is therefore 0.0067 Hz. The coherence is calculated for N range gates located between a distance r_{min} and r_{max} from the lidar. For a fixed crosswind separation d and radial distance from the lidar r, N_d estimates of the coherence are calculated. In total, $N_d \times N$ coherence estimates are obtained, and are denoted Γ_q^j, where $j = \{1, ..., N_d\}$ and $q = \{1, ..., N\}$. By assuming that the coherence does not significantly evolve between r_{min} and r_{max}, it is averaged over the N range gates following Eq. 13. This aims to further reduce the uncertainties due to measurement noise and the bias of the estimated root-coherence.

$$\gamma_u(f, d) = \frac{1}{N_d}\frac{1}{N}\sum_{j=1}^{N_d}\sum_{q=1}^{N}\Gamma_q^j(d, f) \tag{13}$$

Two spectral coherence models are compared to the measured coherence. The first one is the IEC coherence model [29] which was used for wind turbines by e.g. [5,30]. The IEC root-coherence is calculated as a function of the frequency f and of the magnitude d of the projection of the separation vector between the two measurement points onto a plane perpendicular to the flow:

$$\gamma_u(f, d) = exp\left\{-12\left[\left(\frac{fd}{\overline{U}_{\mathrm{hub}}}\right)^2 + \left(0.12\frac{d}{8.1\Lambda_1}\right)^2\right]^{0.5}\right\} \tag{14}$$

where $\overline{U}_{\mathrm{hub}}$ is the mean wind velocity recorded at hub height, $\Lambda_1 = 8.1L_c$ and

$$L_c = \begin{cases} 0.7z & \text{if } z \le 60\mathrm{m} \\ 42\mathrm{m} & \text{if } z \ge 60\mathrm{m} \end{cases} \tag{15}$$

The Frøya coherence model, used for offshore wind by Andersen and Løvseth [6], is the second one investigated in the present study. The root-coherence γ_u measured at two altitude z_p and z_q is expressed as a function of the frequency

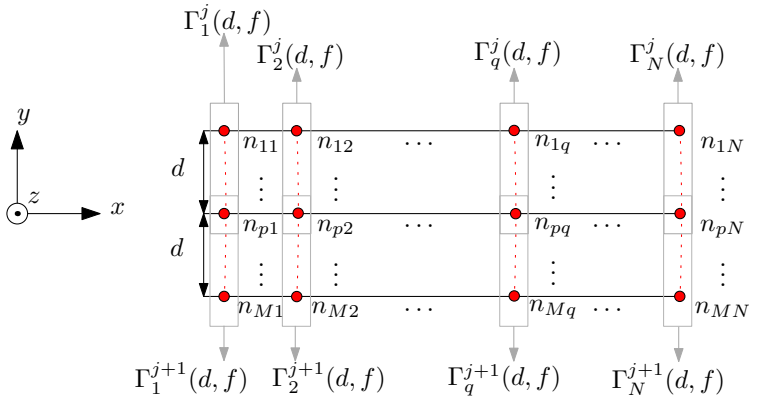

Fig. 4. Multiple estimates of the root-coherence are calculated for a given cross-flow separation d, by monitoring $M \times N$ volumes (red dots) denoted n_{pq} where $p = \{1, 2, \ldots, M\}$ and $q = \{1, 2, \ldots, N\}$.

f, the spatial separation Δ_i, and additional parameters q_i, p_i, r_i, α_i, where $i = \{1, 2, 3\}$ refers to the spatial orientation. These parameters are defined for a reference height of 10 m and provided by Andersen and Løvseth [6]. The Frøya coherence model is:

$$\gamma_u(f) = exp\left\{-\left[\sum_{i=1}^{3}(f/f_{0i})^{2r_i}\right]^{0.5}\right\} \tag{16}$$

where :

$$\begin{aligned} f_{0i} &= \left(\frac{U_{\text{ref}} z_g^{p_i}}{\alpha_i \Delta_i^{q_i}}\right)^{1/r_i} \\ z_g &= \frac{\sqrt{z_p z_q}}{z_{\text{ref}}} \end{aligned} \tag{17}$$

where U_{ref} is the reference wind velocity measured at a reference altitude z_{ref} equal to 10 m. The mean wind velocity is recorded by the anemometers located on FINO1 platform at seven altitudes ranging from 33 to 90 m. The value of U_{ref} is therefore extrapolated by fitting Eq. 18 to the vertical mean velocity profile. The result of the fitting process is an estimation of U_{ref} and of the surface drag coefficient C_d introduced by Charnock [31].

$$U(z) = U_{\text{ref}}\left[1 + \frac{C_d^{1/2}}{0.4}\ln\left(\frac{z}{z_{\text{ref}}}\right)\right] \tag{18}$$

3. Results

3.1. Mean wind velocity and turbulence intensities

3.1.1. RHI scan

To illustrate how the WindCube 100S resolves the mean wind velocity and the turbulence intensity in the vertical plane, we have selected one RHI scan carried out on 20/12/2015 between 06:10 and 06:20. This step is important to assess the homogeneity of the flow, which is a prerequisite to properly calculate the coherence. Comparisons between the lidar data and anemometers measurements located at FINO1 are shown in Table 2 and suggest that the azimuth selected is well aligned with the mean wind direction. We should note that the mean wind velocity reported in Table 2 for the WindCube at an altitude of 33 m is recorded 475 m from FINO1, and the value at an altitude of 90 m is recorded 1.3 km from FINO1. The mean wind velocity and turbulence intensity for the different elevation angles and radial distances are displayed in Fig. 5, where the vertical mean wind velocity profile appears rather uniform along r. The turbulence intensity fluctuates however both with the elevation angles and with r, with values ranging from 4.5 % to

Table 2. Mean wind velocity recorded by the RHI scan and the sonic anemometers on the FINO1 platform (18/12/2015 from 06:10 to 06:20).

	Altitude	33 m		90 m	
		$\overline{U}$ (m s^{-1})	Dir (°)	$\overline{U}$ (m s^{-1})	Dir (°)
Sensors	Sonics on FINO1	12.4	211	14.5	209
	WindCube 100S	13.4	211	14.9	211

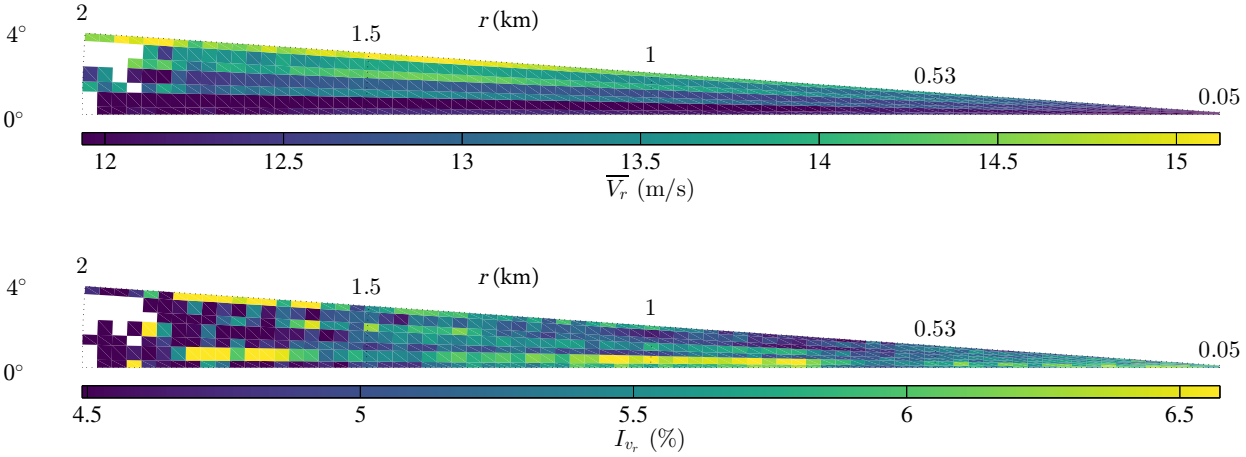

Fig. 5. Mean velocity (top) and turbulence intensity (bottom) for the radial wind component recorded during the RHI scan carried out between 06:10:05 and 06:19:55 on 20/12/2015.

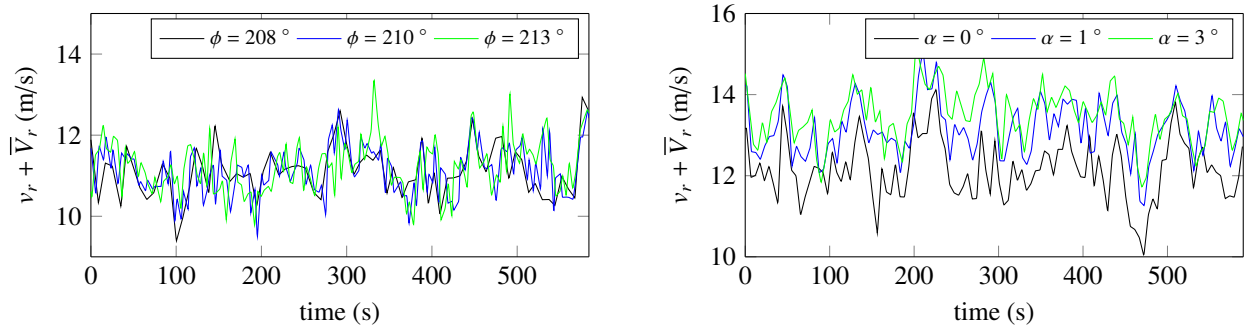

Fig. 6. Time series recorded for r = 1.5 km during the PPI scan carried out on 18/12/2015 from 20:40:07 to 20:49:59 (left) and during the RHI scan conducted on 20/12/2015 from 06:10:02 to 06:19:55 (right).

7% in the area located less than 1 km from the lidar. These values are in the same order of magnitude as those found by e.g. [32,33]. For distance from FINO1 larger than 1.5 km, the turbulence intensity and the mean wind velocity are unlikely to be reliable because of the low CNR recorded.

3.1.2. PPI scan

The Selected PPI scan is recorded on 18/12/2015, between 20:40 and 20:50. The elevation angle was fixed to 0° and six azimuth angles ranging from 208° to 214° were used. According to the anemometer located 33 m above the sea at the FINO1 platform, the wind direction during that period was S-SW with a mean value of 210° and a mean wind velocity of 11.7 m s^{-1}. The mean wind velocity recorded during this PPI scan, at an altitude of 25 m, for an azimuth angle of 211° and a distance of 100 m from the lidar was 11.1 m s^{-1}. This is in good agreement with the anemometer

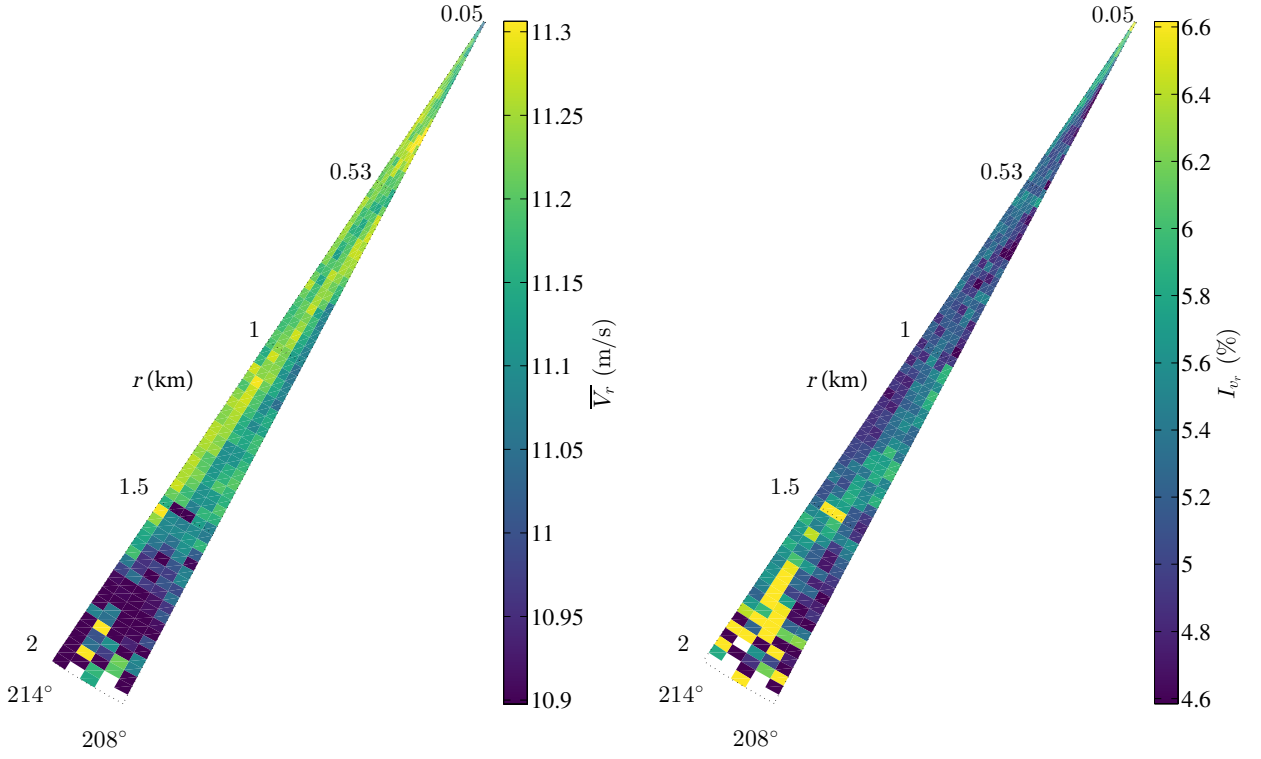

Fig. 7. Mean velocity (left) and turbulence intensity (right) for the radial wind component recorded during the PPI scan between 20:40:07 and 20:49:59 on 18/12/2015.

data indicating that the lidar is properly measuring the along-wind velocity component. The mean wind velocity and its turbulence intensity is displayed for the entire scanned area in Fig. 7. A rather uniform mean wind velocity field is observed, but small fluctuations of the radial mean wind velocity of about 0.3 m s^{-1} are visible, and may be due to the far wakes of the wind turbines located to the South and South-West of FINO1. The turbulence intensity seems to capture a small part of these wakes, with locally slightly increasing values. A low CNR is also obtained for distances larger than 1.5 km. In the following, wind turbulence is therefore analysed for radial distances r ranging from 50 m to 1.5 km for both the PPI and RHI scanning modes.

Time series recorded during the PPI scan and the RHI scan are compared in Fig. 6. For the PPI scan, the mean wind velocity is recorded with discrepancies lower than 0.05 m s^{-1} between the different azimuths angles. The zero elevation angle used shows that the horizontal flow is uniform over the separation studied, which is in agreement with Fig. 7. For the RHI scan, Fig. 6 shows mean wind velocities of 12.1 m s^{-1}, 13.1 m s^{-1} and 13.5 m s^{-1} for elevations angles of 0°, 1° and 3° respectively.

3.2. Turbulence length scales

The along-wind turbulence length scales (Eq. 10) have also been estimated from the lidar data, by taking advantage of the relatively high sampling rate (Fig. 8 and 9). For the PPI scan, the turbulence length scales are quite uniform along the radial distances, with values ranging from 65 to 115 metres, indicating that the single point spectra may also be quite uniform. For the RHI scan, rather uniform integral length scales are also observed, except for elevation between 3° and 4° and for a distance between 800 m and 1.2 km from the lidar, where length scales larger than 140 m are measured. This is due to measurement noise, not well understood at present.

For each given radial distance r, the crosswind turbulence length scales can be calculated by using the wind velocity measured for multiple crosswind separations, and their evolutions with r are displayed in Fig. 10. Because these length scales are calculated for different time series corresponding to two different wind conditions, their comparison is not

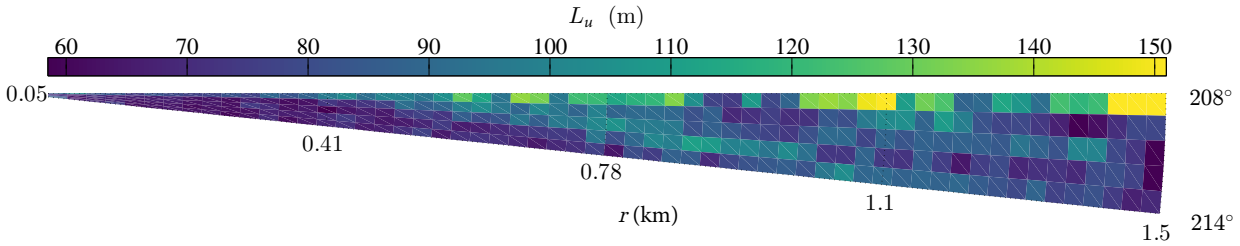

Fig. 8. Along-wind turbulence length scale based on data provided by the PPI scan carried out on 18/12/2015, between 20:40:07 and 20:49:59.

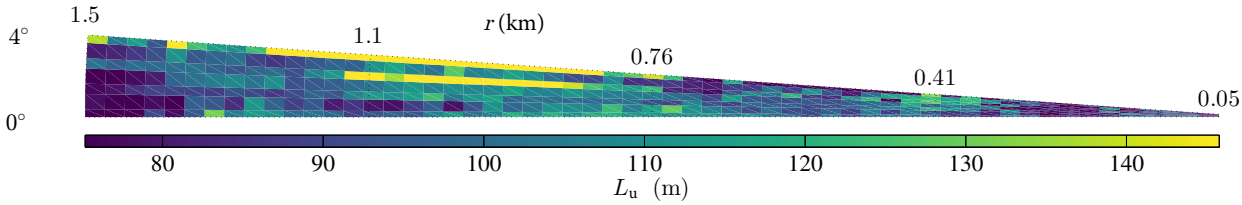

Fig. 9. Along-wind turbulence length scale based on data provided by the RHI scan carried out on 18/12/2015, between 06:10:05 and 06:19:55.

straightforward. The length scale L_u^y from the PPI scan is remarkably uniform, which is consistent with results from subsection 3.1. The length scale L_u^z from the RHI scan is fairly uniform between $r = 500$ m to $r = 1500$ m only.

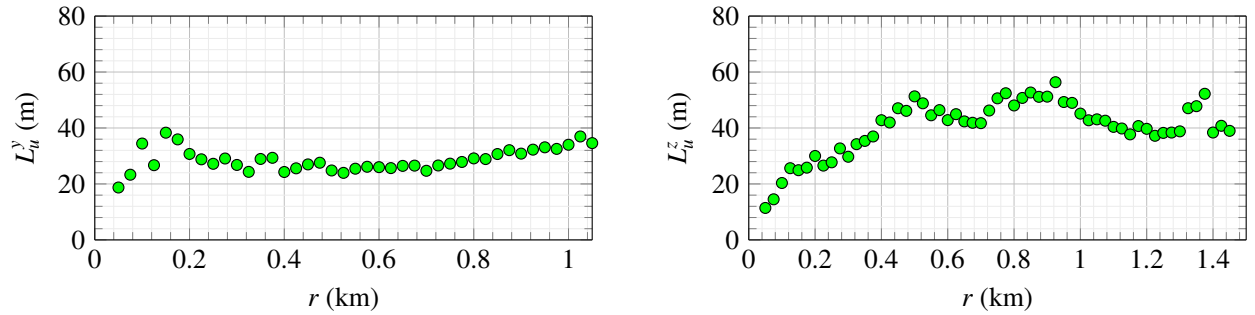

Fig. 10. Evolution of L_u^y (left) and L_u^z (right) with the radial distance based on data from the PPI and RHI scan respectively.

3.3. Coherence from the PPI and RHI scan

In the present study, the root-coherence is calculated for mean wind velocities ranging from 11 to 15 m s^{-1} at an altitude of 25 m. This corresponds to wind velocity between 14 and 18 m s^{-1} at an altitude of 90 m. To obtain robust estimates of the root-coherence, multiple time series of duration 10-minutes, recorded from the period 18/12/2015 to 23/12/2015 are used. Variable wind directions and the fixed central scanning azimuth angle of 211° lead to a potential misalignment between the mean wind direction and the scanning pattern. This introduces an additional error to the one due to the approximations made for the scanning pattern itself (cf. subsection 2.2), and should therefore be as small as possible. The choice of a corresponding acceptable misalignment threshold is therefore a compromise between the number of scans available for the coherence estimation and the additional error, both increasing with this threshold value. To test the sensitivity of our method, we used two different values for the misalignment tolerance:

- $\beta_a \leq 2°$: In that case the coherence can be calculated from 6 PPI and 7 RHI scans.
- $\beta_a \leq 5°$: In that case the amount of available samples for the coherence calculation is increased to 24 PPI scans and 24 RHI scans.

The reference direction for the PPI scans is obtained from the anemometer located 33 m above the sea at the FINO1 platform. For the RHI scan, the average wind direction obtained from the anemometers located at 33, 40, 50, 60, 70, 80 and 90 m above the sea is used. For each selected sample, the logarithmic law in equation 18 agreed well with the measured vertical mean wind profile, and the reference wind U_{ref} was utilized as representative of undisturbed flow conditions.

The root-coherence is calculated for four lateral and vertical separations ranging from 20 to 85 m and presented in Figs. 11 and 12. Larger crosswind separations were measured (up to 150 m for the PPI scan), but a higher number of samples is required to improve their reliability, and such data are therefore not displayed in the present study. To consider only the case where the coherence fluctuates little with increasing distances from the lidar, any scan displaying a standard deviation for L_u^y or L_u^z larger than 30 m is dismissed. For each sample, the measured root-coherence is averaged over radial distances ranging from r_{min} = 500 m and r_{max} = 1500 m from the lidar, following the method proposed in subsection 2.4 .

The measured lateral coherence is compared to the IEC (Kaimal) and Frøya coherence models, both calculated using the reference mean wind speed at the altitude of 25 m and 90 m. The latter is the hub height of the wind turbines located in the Alpha Ventus wind park, on the East side of the FINO1 platform, and is introduced to relate the present data to the IEC coherence model in a consistent manner. The Frøya coherence model is based on the 40 minutes wind records, corrected for the synoptic processes. The present data (10-min time-series) have not been processed in the same manner, but the Frøya data treatment has been approached by excluding the non-stationary data. The IEC Kaimal coherence model for turbulence acting on the entire rotor disc area is given in terms of the mean wind velocity at the hub height as the reference wind speed. For the comparison of the vertical coherence results, the Frøya model is presented for the height of 90 m only. The coherence in the Frøya model is given as a function of the vertical separation combined with the varying associated reference height z_g (see Eq. 17), which does not make it plausible to combine large vertical separations, of e.g. 60 m, with the reference height of z = 25m.

For lateral and vertical separations around 20 m, the measured root-coherence agrees well with the IEC coherence model, but when the crosswind separation increases, the measured root-coherence is lower than predicted by the standard. For the PPI scan, this is observed at every frequency recorded, whereas for the RHI scan, this occurs mainly at frequencies below 0.02 Hz. For vertical separations between 20 m and 60 m, the measured root-coherence agrees

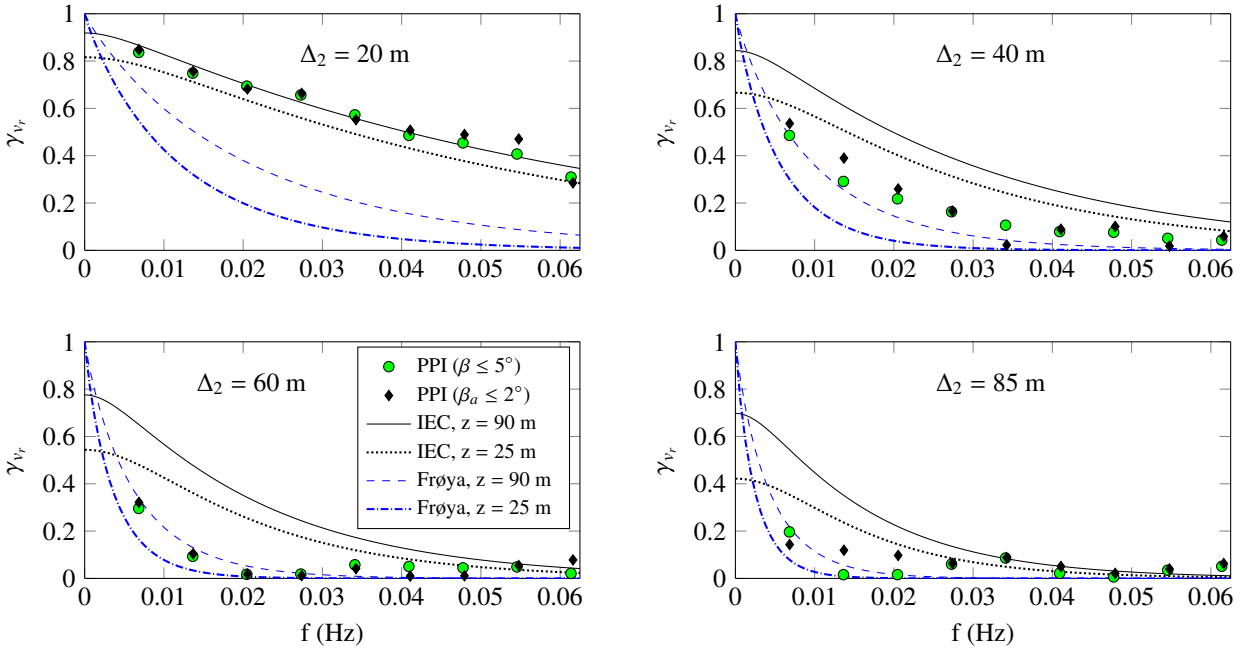

Fig. 11. Root-coherence for lateral separations Δ_2 averaged over data with a mean wind velocities ranging from 11 to 15 m s^{-1} at z = 25 m.

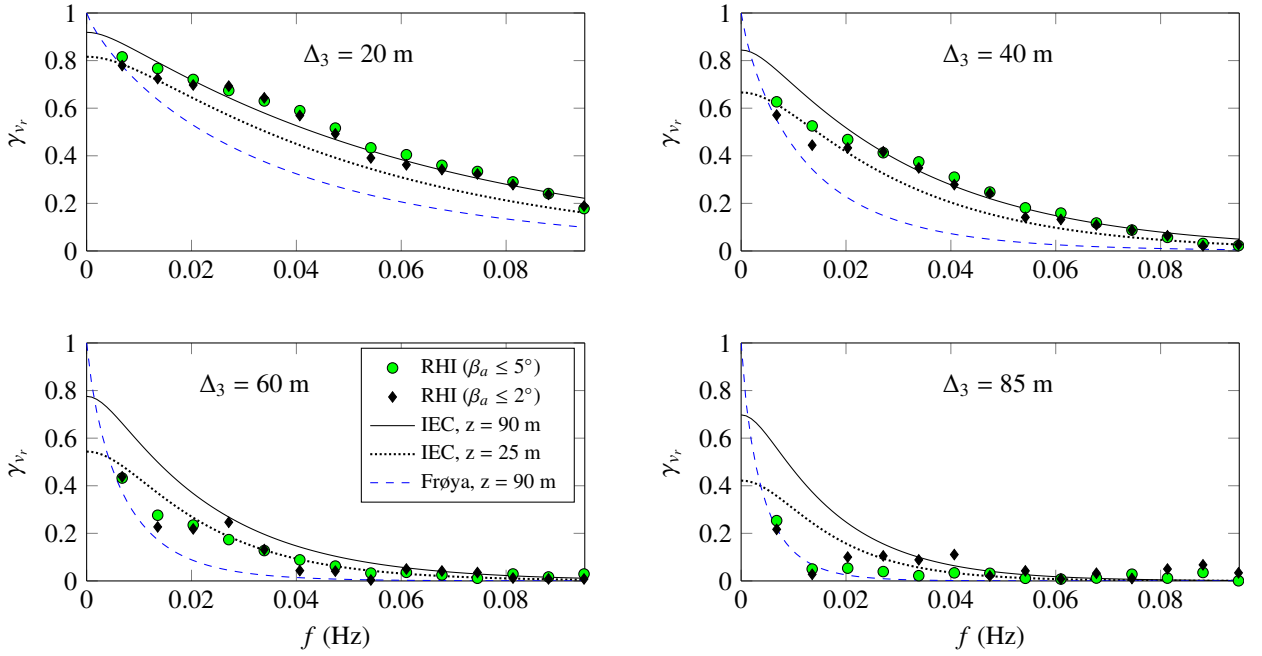

Fig. 12. Root-coherence for vertical separations Δ_3 averaged over data with a mean wind velocities ranging from 11 to 15 m s^{-1} at z = 25 m.

rather well with the IEC coherence model, which is less the case for lateral-separations where a systematic discrepancy is visible. For vertical separations larger than 60 m and lateral separations larger than 40 m, the measured coherence agrees fairly well with the Frøya model. The present data set indicates a lower lateral coherence compared to the vertical one, as in the Frøya measurements [6]. For the measured coherence, the two misalignment thresholds show little difference. This indicates that a value of 5° may be used to increase the statistical significance of the coherence measurement by using more samples.

To better capture the evolution of the coherence at frequency below 0.0067 Hz, longer wind records may be considered. This should overcome the issue of an insufficient smoothing of the root-coherence at large crosswind separations, increase the frequency resolution, and decrease the value of the lowest frequency recorded.

3.4. Challenges and prospects

The present study aimed to monitor the undisturbed flow conditions, but the far wake of a wind turbine was actually recorded. However, the measured root-coherence is expected to be affected by the wake only to a limited degree. Firstly because the wake was more or less aligned with the beams, and secondly because the monitored area was at a distance from 18 to 30 rotor diameters, which is far enough to assume that the wake has little influence on the lateral and vertical coherence [7,34]. The choice of proper wind conditions to study wind coherence with a pulsed Doppler wind lidar is therefore fundamental to obtain reliable estimates. One challenge is to align the scanning beam with the wind direction, which was not automated in the present study. The automation of the lidar alignment may considerably increase the availability of wind records.

If the yaw angle between the beam and the wind direction increases, the lidar may record wind turbine wakes that are not aligned with the beam. During the RHI scan carried out on 18/12/2015, between 13:50:00 and 13:59:57, a yaw angle of 14° was recorded, and the wakes of at least two upstream wind turbines were likely encountered by the lidar beam, as seen in Fig. 13. A clear velocity deficit is visible for r = 0.5 km and r = 1.8 km, although the quality of the recorded radial velocity becomes low for radial distance over 1.5 km. By using the WindCube 100S and much larger sweeping angles, Kumer et al. [19] have recorded mean wind velocity deficits of 30 % in the far wake area (> 5D) of multiples wind turbines. For the sample displayed on the right panel of Fig. 13, the velocity deficits is around 10 %. The crosswind turbulence length scales L_u^z and L_u^y show sudden variations where the velocity deficit is highest (Fig. 14).

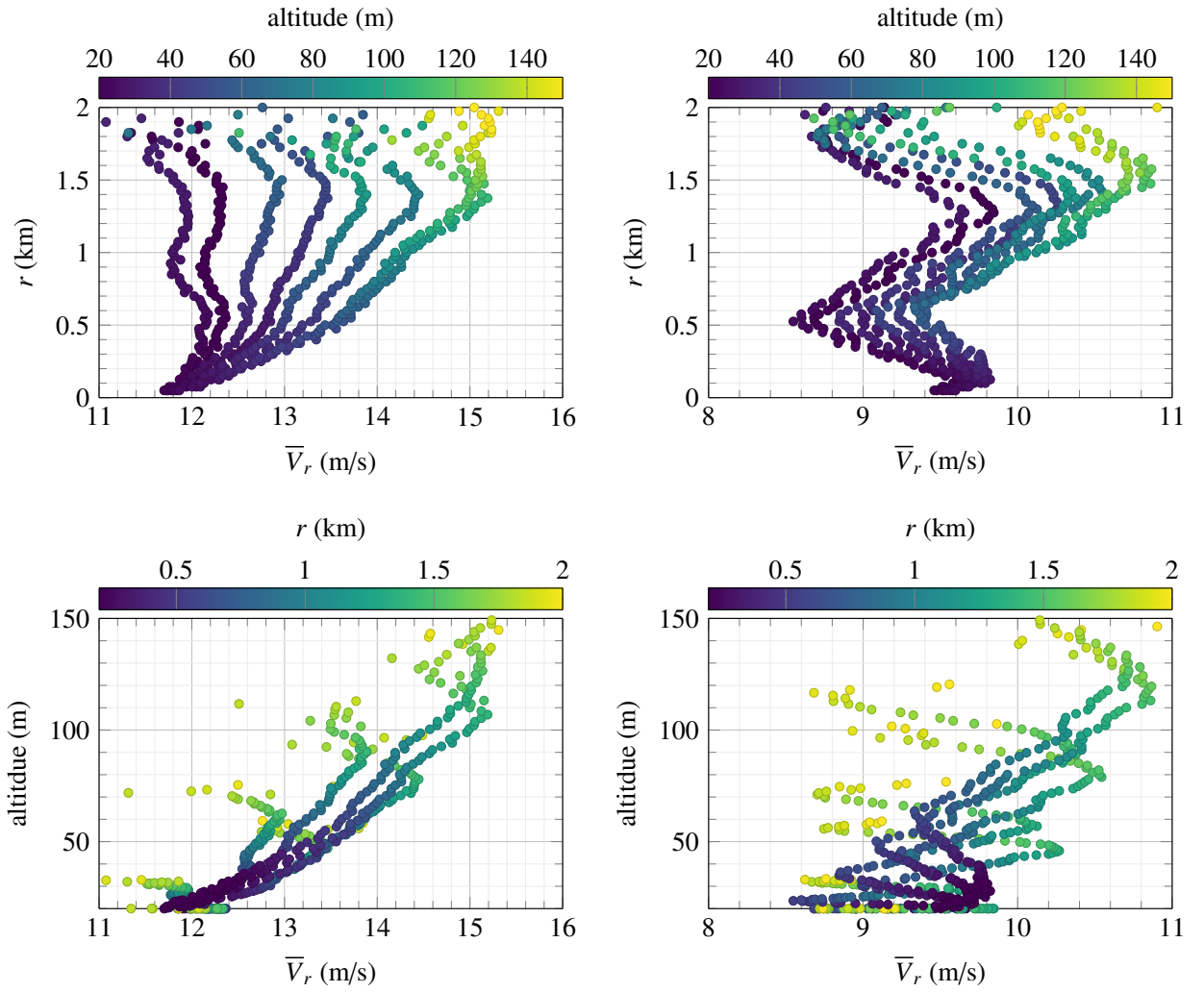

Fig. 13. Mean radial wind velocity profile for the RHI scan recorded between 06:10 and 06:20 (top and bottom left) and between 13:50 and 14:00 on 18/12/2015 (top and bottom right). Multiple "dotted lines" are visible and correspond to the different elevation angles used during the RHI scan.

The largest velocity deficit occurs 500 m from the lidar, which corresponds on Fig. 14 to the radial distance where L_u^z drops from 60 m to 20 m, and L_u^y fluctuates between 25 and 70 m. Such variations indicate the absence of flow homogeneity, which is a prerequisite for coherence estimation.

The estimation of the error due to the volume averaging effect, previously highlighted for the WindCube 100S [10], is another challenge. The normalization of the cross-spectral densities and the low frequencies recorded in the present study should limit the influence of beam averaging on the coherence measurement. However, the volume averaging due to the sweeping of the beam may also establish a minimal crosswind separation below which the coherence is not reliable, and has yet to be decided. In the present study, a minimal crosswind separation of 20 m was used, assumed large enough to provide reliable estimates of the root-coherence.

The present study aimed at demonstrating the potential of a wind lidar to measure wind coherence, although it is clear that many more samples are required to characterize offshore wind coherence in more details. For example, the atmospheric stability may have some influence on the "dissolution" of the far-wake measured by the Lidar. Under stable atmospheric conditions, Hansen et al. [35] observed that the power deficit due to wind turbines wake is much larger, due to less effective turbulence mixing. In other words, the assumption of undisturbed flow is more challenged under stable atmospheric conditions, and the coherence itself is influenced by atmospheric stability [1].

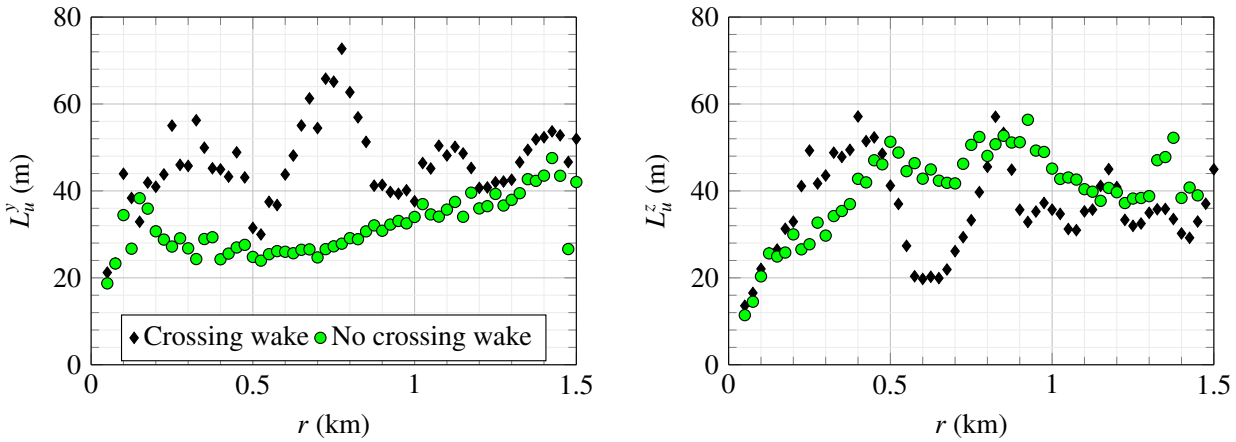

Fig. 14. Influence of the far-wake of wind turbines crossing the beam on the cross-flow turbulence length scale L_u^y (PPI scan) and L_u^z (RHI scan).

In the present study, the monitored frequencies range from 0.0067 Hz to 0.065 Hz (PPI scan) and from 0.0067 Hz to 0.095 Hz (RHI scan). Such frequencies are relevant for dynamic analysis of offshore wind turbines in deep waters. For example, the rigid body motion of a floating wind turbine, such as the Hywind concept, has surge and pitch resonant responses at frequencies below 0.1 Hz [36]. Another study carried out by Coulling et al. [37] on the NREL 5-MW reference wind turbine mounted on a floating platform also showed that the "global" dynamic response of the model was at frequencies below 0.1 Hz. For a bottom-fixed tower, larger eigen-frequencies are relevant, as seen for e.g. the NREL 5-MW reference wind turbine [38]. In that case, a system of two lidars, using slightly divergent LOS scans may be used to estimate the wind coherence for frequencies up to 0.5 Hz.

4. Conclusions

A novel set-up with a single wind lidar was used in December 2015, to study two-point statistics of wind turbulence at the FINO1 platform in the North Sea. This particular configuration, based on small sweeping angles, allowed for the first time a sufficiently high time resolution to test the applicability of pulsed wind lidar in monitoring lateral and vertical wind coherence of the along-wind component.

For cross-flow separation from 20 to 85 m, the preliminary coherence estimates from the PPI and RHI scan showed an overall agreement with the IEC and Frøya coherence models. A more complete description of offshore wind coherence requires a comparison of lidar measurements with sonic anemometers data, and a study of the influence of atmospheric stability on the measured coherence. In case of a wind farm, a detailed analysis of both the undisturbed flow and the flow located in the wake of a wind turbine becomes relevant. Coherence measurement by Doppler wind lidar faces currently two challenges: the ability to efficiently align the scanning beam with the mean wind direction, and the capability to scan the wind field over large distances, with both a high CNR and a low accumulation time.

Acknowledgements

The authors would like to acknowledge the valuable review of the manuscript by Prof. Jónas Snæbjörnsson of Reykjavík University and the University of Stavanger. The lidar data were acquired as part of the OBLO measurement campaign (project number: 227777), performed by the Norwegian Center for Offshore Wind Energy NORCOWE, funded by The Research Council of Norway (project number: 193821).

References

[1] Kristensen, L., Jensen, N.. Lateral coherence in isotropic turbulence and in the natural wind. Boundary-Layer Meteorology 1979;17(3):353–373. doi:10.1007/BF00117924.

[2] Toriumi, R., Katsuchi, H., Furuya, N.. A study on spatial correlation of natural wind. Journal of Wind Engineering and Industrial Aerodynamics 2000;87(23):203 – 216. doi:10.1016/S0167-6105(00)00037-4; 10th International Conference on Wind Engineering.

[3] Hui, M., Larsen, A., Xiang, H.. Wind turbulence characteristics study at the Stonecutters Bridge site: Part II: Wind power spectra, integral length scales and coherences. Journal of Wind Engineering and Industrial Aerodynamics 2009;97(1):48 – 59. doi:10.1016/j.jweia.2008.11.003.

[4] Bowen, A.J., Flay, R.G.J., Panofsky, H.A.. Vertical coherence and phase delay between wind components in strong winds below 20 m. Boundary-Layer Meteorology 1983;26(4):313–324. doi:10.1007/BF00119530.

[5] Saranyasoontorn, K., Manuel, L., Veers, P.S.. A comparison of standard coherence models for inflow turbulence with estimates from field measurements. Journal of Solar Energy Engineering 2004;126(4):1069–1082. doi:10.1115/1.1797978.

[6] Andersen, O.J., Løvseth, J.. The frøya database and maritime boundary layer wind description. Marine Structures 2006;19(23):173 – 192. doi:10.1016/j.marstruc.2006.07.003.

[7] Højstrup, J.. Spectral coherence in wind turbine wakes. Journal of Wind Engineering and Industrial Aerodynamics 1999;80(12):137 – 146. doi:10.1016/S0167-6105(98)00198-6.

[8] Mikkelsen, T., Mann, J., Courtney, M.. Wind scanner: A full-scale laser facility for wind and turbulence measurements around large wind turbines. In: European Wind Energy Conference and Exhibition 2008. European Wind Energy Association (EWEA); 2008,.

[9] Mikkelsen, T., Mann, J., Courtney, M., Sjöholm, M.. Windscanner: 3-d wind and turbulence measurements from three steerable doppler lidars. IOP Conference Series: Earth and Environmental Science 2008;1:U148–U156. doi:10.1088/1755-1307/1/1/012018.

[10] Mann, J., Cariou, J.P.C., Parmentier, R.M., Wagner, R., Lindelöw, P., Sjöholm, M., et al. Comparison of 3d turbulence measurements using three staring wind lidars and a sonic anemometer. Meteorologische Zeitschrift 2009;18(2):135–140. doi:10.1127/0941-2948/2009/0370.

[11] Jakobsen, J.B., Cheynet, E., Snæbjörnsson, J., Mikkelsen, T.K., Sjöholm, M., Angelou, N., et al. Assessment of wind conditions at a fjord inlet by complementary use of sonic anemometers and lidars. Energy Procedia 2015;80:411 – 421. doi:10.1016/j.egypro.2015.11.445; 12th Deep Sea Offshore Wind R&D Conference, EERA DeepWind'2015.

[12] Lothon, M., Lenschow, D., Mayor, S.. Coherence and scale of vertical velocity in the convective boundary layer from a doppler lidar. Boundary-Layer Meteorology 2006;121(3):521–536. doi:10.1007/s10546-006-9077-1.

[13] Kristensen, L., Kirkegaard, P., Mann, J., Mikkelsen, T., Nielsen, M., Sjöholm, M.. Spectral coherence along a lidar-anemometer beam. Tech. Rep.; Danmarks Tekniske Universitet, Risø Nationallaboratoriet for Bæredygtig Energi; 2010.

[14] Kindler, D., Oldroyd, A., MacAskill, A., Finch, D.. An eight month test campaign of the Qinetiq ZephIR system: Preliminary results. Meteorologische Zeitschrift 2007;16. doi:10.1127/0941-2948/2007/0226.

[15] Canadillas, B., Bégué, A., Neumann, T.. Comparison of turbulence spectra derived from lidar and sonic measurements at the offshore platform FINO1. In: Proceedings of the 10th German Wind Energy Conference, DEWEK. 2010,.

[16] Jacobsen, S., Lehner, S., Hieronimus, J., Schneemann, J., Kühn, M.. Joint offshore wind field monitoring with spaceborne sar and platform-based doppler lidar measurements. The International Archives of Photogrammetry, Remote Sensing and Spatial Information Sciences 2015;40(7):959.

[17] Trabucchi, D., Steinfeld, G., Bastine, D., Trujillo, J.J., Schneemann, J., Khn, M.. Study of wake meandering by means of fixed point lidar measurements: Spectral analysis of line-of-sight wind component. Journal of Physics: Conference Series 2015;625(1):012016. doi:10.1088/1742-6596/625/1/012016.

[18] Kumer, V.M., Reuder, J., Furevik, B.R.. A comparison of lidar and radiosonde wind measurements. Energy Procedia 2014;53:214–220. doi:10.1016/j.egypro.2014.07.230.

[19] Kumer, V.M., Reuder, J., Svardal, B., Stre, C., Eecen, P.. Characterisation of single wind turbine wakes with static and scanning wintwex-w lidar data. Energy Procedia 2015;80:245 – 254. doi:10.1016/j.egypro.2015.11.428; 12th Deep Sea Offshore Wind R&D Conference, EERA DeepWind'2015.

[20] Teunissen, H.. Structure of mean winds and turbulence in the planetary boundary layer over rural terrain. Boundary-Layer Meteorology 1980;19(2):187–221. doi:10.1007/BF00117220.

[21] Holmes, J.. Wind Loading of Structures, Third Edition. CRC Press; 2015. ISBN 9781482229226.

[22] Taylor, G.I.. Diffusion by continuous movements. Proceedings of the London Mathematical Society 1922;s2-20(1):196–212. doi:10.1112/plms/s2-20.1.196.

[23] Lenschow, D.H., Boba Stankov, B.. Length Scales in the Convective Boundary Layer. Journal of Atmospheric Sciences 1986;43:1198–1209. doi:10.1175/1520-0469(1986)043<1198:LSITCB>2.0.CO;2.

[24] Pearson, G., Davies, F., Collier, C.. An analysis of the performance of the ufam pulsed doppler lidar for observing the boundary layer. Journal of Atmospheric and Oceanic Technology 2009;26(2):240–250. doi:10.1175/2008JTECHA1128.1.

[25] Davenport, A.G.. The spectrum of horizontal gustiness near the ground in high winds. Quarterly Journal of the Royal Meteorological Society 1961;87(372):194–211. doi:10.1002/qj.49708737208.

[26] Davenport, A.G.. The response of slender, line-like structures to a gusty wind. Proceedings of the Institution of Civil Engineers 1962;23(3):389–408. doi:10.1680/iicep.1962.10876.

[27] Welch, P.D.. The use of fast Fourier transform for the estimation of power spectra: A method based on time averaging over short, modified periodograms. IEEE Trans Audio Electroacoustics 1967;15:70–73. doi:10.1109/TAU.1967.1161901.

[28] Carter, G., Knapp, C., Nuttall, A.H.. Estimation of the magnitude-squared coherence function via overlapped fast fourier transform processing. Audio and Electroacoustics, IEEE Transactions on 1973;21(4):337–344. doi:10.1109/TAU.1973.1162496.

[29] IEC 61400-1, . IEC 61400-1 Wind turbines Part 1: Design requirements; 2005.
[30] Jonkman, B.J.. Turbsim user's guide: Version 1.50. 2009.
[31] Charnock, H.. Wind stress on a water surface. Quarterly Journal of the Royal Meteorological Society 1955;81(350):639–640. doi:10.1002/qj.49708135027.
[32] Barthelmie, R.. Monitoring offshore wind and turbulence characteristics in Denmark. Wind Energy 1999: Wind Power Comes of Age 2000;:311–321.
[33] Türk, M., Emeis, S.. The dependence of offshore turbulence intensity on wind speed. Journal of Wind Engineering and Industrial Aerodynamics 2010;98(89):466 – 471. doi:10.1016/j.jweia.2010.02.005.
[34] Jimenez, A., Crespo, A., Migoya, E., Garcia, J.. Large-eddy simulation of spectral coherence in a wind turbine wake. Environmental Research Letters 2008;3(1):015004. doi:10.1088/1748-9326/3/1/015004.
[35] Hansen, K.S., Barthelmie, R.J., Jensen, L.E., Sommer, A.. The impact of turbulence intensity and atmospheric stability on power deficits due to wind turbine wakes at horns rev wind farm. Wind Energy 2012;15(1):183–196. doi:10.1002/we.512.
[36] Nielsen, F.G., Hanson, T.D., Skaare, B.. Integrated dynamic analysis of floating offshore wind turbines. In: 25th International Conference on Offshore Mechanics and Arctic Engineering. American Society of Mechanical Engineers; 2006, p. 671–679. doi:10.1115/omae2006-92291.
[37] Coulling, A.J., Goupee, A.J., Robertson, A.N., Jonkman, J.M., Dagher, H.J.. Validation of a fast semi-submersible floating wind turbine numerical model with deepcwind test data. Journal of Renewable and Sustainable Energy 2013;5(2):023116. doi:10.1063/1.4796197.
[38] Jonkman, J., of Colorado at Boulder. Aerospace Engineering, U.. Dynamics Modeling and Loads Analysis of an Offshore Floating Wind Turbine. University of Colorado at Boulder; 2007. ISBN 9780549315490.